ORIGINAL ARTICLE

A numerical approach to determine the intrinsic attenuation of concrete

Erik H. Saenger · Martin Balcewicz · Giao Vu · Eva Jägle · Jithender Timothy · Claudia Finger

Received: 16 April 2025 / Revised: 19 November 2025 / Accepted: 28 December 2025 / Published online: 30 January 2026
© The Author(s) 2026

Abstract
Ultrasound measurements are used for monitoring the structural health of concrete. The elastic waves propagating in concrete structures are attenuated by scattering and intrinsic attenuation. Both quantities have to be determined for a detailed material characterization and for realistic numerical simulations of wave propagation in such structures. We present in this paper a numerical approach to determine the intrinsic attenuation of concrete. For this purpose, a realistic digital three-dimensional concrete specimen is created that accounts for correct volume fractions of aggregates of different sizes embedded into a mortar matrix. Using a viscoelastic finite difference scheme, we perform simulations of the ultrasound wave field in these digital models with different attenuation levels. The numerical observations are compared with results from ultrasonic measurements on a sample of saturated concrete to estimate the intrinsic attenuation. Embedded sensors are used for those long-term laboratory experiments. For this saturated concrete, we obtain Q=130 in a frequency band around 60 kHz.

Keywords Concrete · Ultrasound · Intrinsic attenuation · Measurement · Numerical simulation

1 Introduction

Concrete consists of different constituents such as aggregate grains of arbitrary shapes, air voids and the cement paste matrix and, hence, is a strongly heterogeneous material. Every concrete mix is unique due to the arbitrary distribution of grains in the casting form and an unknown content of air inclusions that cannot be eliminated completely by compaction. From the 1990s onward, numerical simulations that can investigate mesoscopic-level material response have been reported [22]. The inclusion of mesoscopic structures in concrete, especially the distribution and shape of aggregates, has led to the accurate modeling of the propagation of ultrasonic waves. Examples are the 2D scattering study by Chekroun et al. [5], the combined laboratory and numerical considerations by Iliopoulos et al. [12], the finite-element simulations by Yu et al. [33], and the acoustic emission investigations by Livitsanos et al. [20].

As pointed out by Philippidis and Aggelis [25], ultrasound signals in concrete (and other strongly heterogeneous materials) can be attenuated by an intrinsic (absorption) mechanism, by an extrinsic (scattering) mechanism, and

Erik H. Saenger, Martin Balcewicz, Giao Vu, Eva Jägle, Jithender Timothy and Claudia Finger have contributed equally to this work.

by geometric attenuation (spreading). While geometric spreading can be corrected, it is not straightforward to distinguish between intrinsic and scattering attenuation in laboratory or other experiments. Therefore, the experimental studies on attenuation in concrete and other materials consider mostly intrinsic and scattering attenuation simultaneously. To cite some instances, there is an experimental study by Abdullah and Sichani [1], a comprehensive collection of attenuation coefficients by Ono [24] and an investigation how to increase the sound absorption in concrete with additives by Cheyne and Thurman [6].

An alternative approach uses a diffusion model to separate absorption from scattering attenuation. This is applied in a survey of cement-based materials by Becker et al. [4] and a concrete microstructure investigation using X-ray computed tomography by Landis et al. [18]. However, this method can only be applied when the diffuse wave approximation is valid (ultrasound wavelength λ is smaller or equal to the scatter size a; e.g. Kim [14]), and it is based on the assumption that the source transducer emits a wave field which is predominantly longitudinal (e.g. Punurai et al. [26]).

The goal of this study is to develop an approach to determine the intrinsic attenuation of concrete without those diffusion-related assumptions. One example is the laboratory experiment reported in this study where the application of the diffusion approach would not be appropriate due to the much larger wavelength compared to the scatter size (see Sect. 2.7). In general, an exact determination of intrinsic attenuation is necessary for a complete material characterization. Moreover, this knowledge can be used to improve the applicability of numerical solvers to study ultrasound in concrete structures.

The paper is structured as follows: In Sect. 2, we describe an ultrasound experiment in a concrete specimen surrounded by air. A specific time-dependent decay of the wave amplitudes can be observed, which depends on the saturation level of the concrete. It is expected that the saturation level will impact the intrinsic attenuation. This is confirmed by theoretical investigations [21] as well as with experimental studies [2]. Therefore, an experimental setup with a high initial saturation is chosen. In Sect. 3, we describe a digital twin of the reported experiment. We apply a finite-difference technique to simulate the wave propagation in the concrete sample. Because we will implement viscoelastic behavior in our numerical experiment, we are able to match the experimental observations. In Sect. 4, an iterative analysis is performed to determine the intrinsic attenuation of concrete. In Sect. 5, we elaborate further steps to improve our suggested methodology.

2 Experimental setup

2.1 Specimen production (25.02.2021)

In the experiment, one single prism-shaped concrete specimen with dimensions of 400 x 100 x 100 mm^3 was produced using ordinary Portland cement (CEM I 52.5 R) with a water-to-cement ratio of 0.60 and crushed quartzitic aggregates sourced from the Taunus region. Pre-tests for the predominantly quartzitic crushed aggregates yielded a Young's modulus of 84.6 GPa and a Poisson's ratio of 0.12. The compressive strength of the aggregates was 368.0 MPa. Aggregates with a maximum grain size of 16 mm were used. The concrete grading curve of the aggregates and the casting process was the same as used in Diewald et al. [7]. The air-void content in the fresh concrete was determined as 1 % with a standardized pressure method. Sufficient concrete workability for good sensor-concrete coupling was verified by means of a consistency test, which yielded a flow spread of 325 mm. The concrete properties were tested 56 days after production yielding a compressive strength of 52.5 MPa and a Young's modulus of 33.5 GPa.

2.2 Curing of specimen before drying

Following its production, the concrete specimen was stored under water for more than 2 years. During this time, the microstructure-forming reaction of the water with the cement took place without a water shortage as drying of

the specimen was prevented. Curing under water further results in a reduced formation of cracks during the hardening process. At the beginning of the experiment, when the specimen was removed from the water, the chemical reaction rate decreased to a negligible level, i.e., the microstructure can be considered to have reached its final state. The mesostructure of the solid concrete specimen is comprised of quartzitic crushed aggregates with sizes up to 16 mm, the solid cement paste matrix, which binds the aggregates together, and pores of different sizes in the nanometer (gelpores), micrometer (capillary pores) and millimeter (coarse pores) range.

2.3 Drying conditions

Drying was carried out with ambient conditions of 20 °C and around 65 % of relative humidity. These conditions align with commonly adopted standards for concrete testing, e.g., [8], and are assumed to ensure drying without the formation of drying-induced damage. To enable air circulation, the specimen is placed on spacers, which ensures a distance of 20 mm between the bottom specimen surface and the shelf. The specimen setup is illustrated in Fig. 1.

2.4 Initial state (31.05.2023)

Due to pre-conditioning (water storage), the specimen is saturated with water. This includes capillary pores as well as larger, coarse pores, but some pores could have remained empty or incompletely filled with water. However, it is assumed that the storage conditions ensured maximum water saturation under real conditions. Immediately after removal of the specimen from the water, the surface is wet and it takes some minutes until the surface visually appears dry.

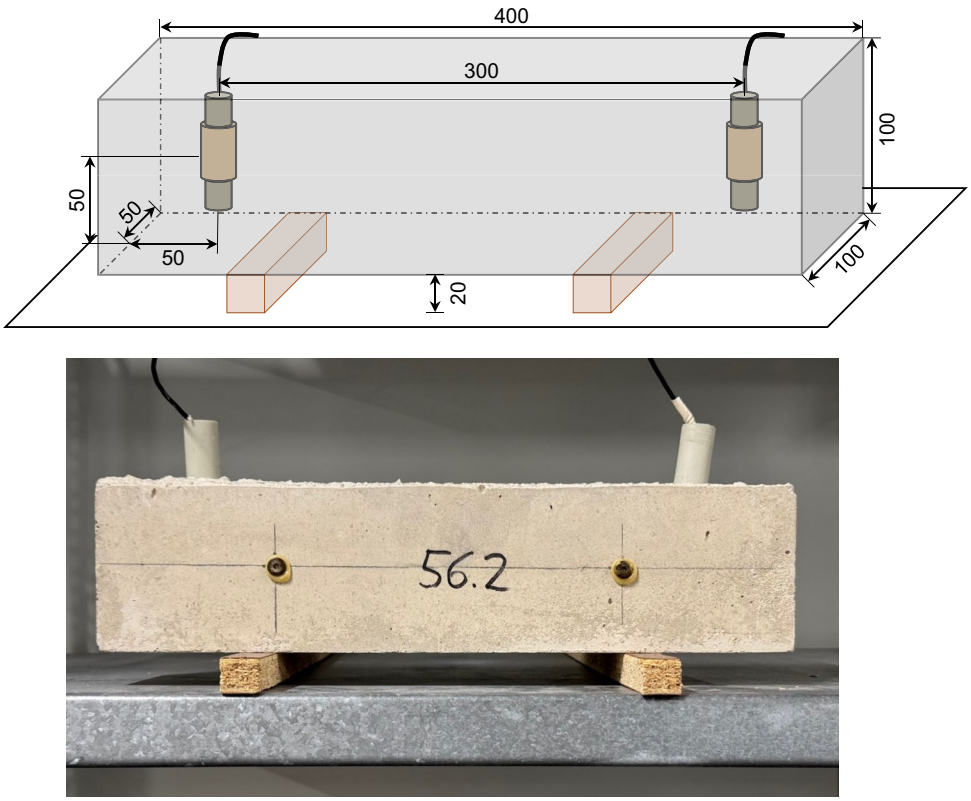

Fig. 1 Experimental setup used for measurement of ultrasonic signals. Schematic plot (top) and real specimen (bottom): Two ultrasound transducers in a concrete specimen (400 x 100 x 100 mm^3). The specimen is placed on spacers, which provide a distance of 20 mm between the shelf and the concrete surface and enable air circulation

2.5 After several days (06.06.2023)

The internal humidity of the specimen has dropped, and the specimen has lost around 0.65 % of its initial weight due to drying. This leads to coarse pores being emptied and then filled with air rather than free water. As the internal humidity of the specimen is generally still high, the gel and most of the capillary pores are still water-filled. However, due to the drying conditions with ambient relative humidity of approximately 65 %, an internal moisture gradient occurs.

2.6 After several weeks (03.08.2023)

The internal moisture level is further reduced, and the specimen weight has decreased around 1.79 % compared to its initial value. While an equilibrium state with the ambient relative humidity has not yet been reached, further moisture loss occurs at a decreasing rate, and the water is removed from the capillary pores with decreasing radii.

2.7 Recording of ultrasound

A schematic plot of our experiment is given in Fig. 1. The embedded piezoelectric transducers (described in Niederleithinger et al. [23]) are used to acquire ultrasonic signals. The transducers acted as sender-receiver pairs with a central frequency of 60 kHz. The wavelengths of the emitted and recorded P-waves of around 70 mm are, therefore, approximately four times larger than the largest aggregates. The measurement system (described in Fontoura Barroso et al. [3]) records signals with 12,000 samples and a sampling rate of 1 MHz. To follow the drying process, the specimen is weighed regularly during the full drying process. Therefore, the transducers must be detached from the measurement system and re-attached to continue ultrasonic signal collection. However, consecutive measurements will demonstrate a high accuracy of the performed experiment (see Appendix A). Ultrasonic signals were collected continuously during the full drying period, with measurements taken approximately every 5 min. Small variations in the interval occurred as a result of variations in the processing time required for each signal. As the transducer needed to be detached from the system to weigh the specimen, signal collection was paused for the manual measurements. At least three signals were collected between these breaks. The ultrasonic signals and further associated data are available in Jägle et al. [13]. In the following, only ultrasonic signals collected for the saturation stages as described above are evaluated.

3 Numerical setup

3.1 Generation of synthetic concrete structures

To generate a highly realistic virtual specimen for simulating the ultrasonic wave propagation, we use the computational tool developed by Holla et al. [11]. Inputs are the measured size distribution of the coarse aggregates and the geometrical descriptions of each aggregate family (e.g., size, aspect ratio, smoothness, concave surface parameters). We use the parameters described in Sect. 2.1. The used model is displayed in Fig. 2; very similar models have also been used in Vu et al. [32].

The digital concrete specimen is modeled as a three-phase composite consisting of mortar matrix, coarse aggregates, and voids. Aggregates of varying sizes are generated according to the AB16 standard size distribution grade with a maximum size of 16 mm. Given the optimal spatial discretization size (0.5 mm), only coarse aggregates larger than 3 mm are explicitly resolved. Consequently, a volume fraction of 40.5 % is achieved. As shown in Fig. 3, the mesoscale model agrees well with the real measurements. Assuming a total volume fraction of 70.79 %, the remaining smaller aggregates ($\varphi = 30.29\,\%$) are implicitly incorporated into the hardening cement matrix. Subsequently, the elastic properties of the mortar matrix are estimated using the Mori Tanaka

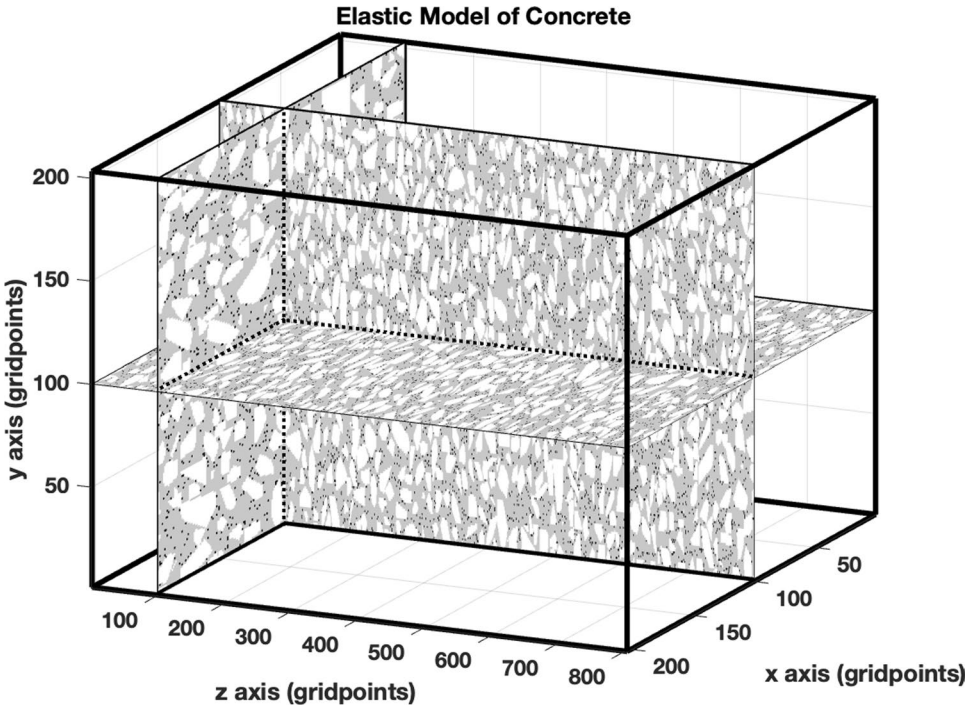

Fig. 2 Digital model of the concrete specimen. White color are aggregates and grey color indicates mortar. Axis labels are given in gridpoints with 1 gridpoint equal to 0.5 mm

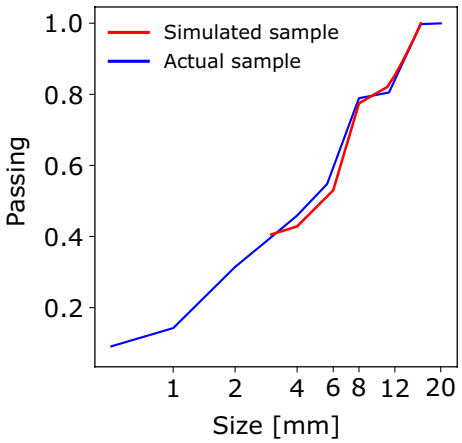

Fig. 3 Comparison of modeled and measured size distributions of coarse quartzitic aggregates in the simulated concrete specimen

homogenization scheme and the value of the cement paste reported in Ulm et al. [31], as listed in Table 2. Additionally, 3 % voids are included. As scatterers, they play a non-negligible role in the diffusivity and wave propagation characteristics.

3.2 Viscoelastic modeling of ultrasound in concrete structures

The rotated staggered finite difference method

We have worked on the application of the rotated staggered grid (RSG) finite-difference (FD) technique [30] to the wave equations for anisotropic media (up to triclinic symmetry [29]). The RSG uses rotated finite-difference operators, leading to a distribution of modeling parameters in an elementary cell where all components of one physical property are located only at one single position. This can be advantageous for modeling wave propagation in anisotropic media or complex media, including high-contrast discontinuities, as no averaging of elastic moduli is needed. The resulting applicability of the RSG in concrete structures was demonstrated in several

studies. For example, in the study of Kocur et al. [15] wave propagation is simulated in a segmented x-ray computed tomography model of a concrete specimen. Moreover, in Saenger [28] time reverse characterization of sources in synthetic 2D concrete samples is demonstrated; this technique was later applied to laboratory acoustic emission experiments in Kocur et al. [16].

General Maxwell body

The implementation of a generalized Maxwell body (GMB) to the RSG technique is described in Saenger et al. [27]. This is a well-known rheological model, which has been previously used to simulate (nearly) frequency-independent attenuation by a time-domain FD scheme in 2D [9] and in 3D [17]. The frequency-dependent elastic moduli $C_{ijkl}(\omega)$ are given by:

$$C_{ijkl}(\omega) = c_{ijkl} - \sum_{m=1}^{n} \tilde{Y}_m^{ijkl} \frac{\omega_m}{i\omega + \omega_m}, \tag{1}$$

with ω as angular frequency, c_{ijkl} as the elastic tensor, n as number of relaxation mechanisms, $\tilde{Y}_m^{ijkl}$ as the tensors of anelastic coefficients and ω_m as angular relaxation frequencies. However, in Saenger et al. [27] the GMB is used to implement a viscous fluid; therefore we describe in Appendix C how to approximate a nearly constant Q behavior with two Maxwell bodies.

The numerical setup

The simulation setup is analogous to the ultrasonic investigation of concrete described in Finger et al. [10] and Vu et al. [32].

The physical size of the concrete specimen is 400 x 100 x 100 mm^3; with a spatial discretization of 0.5 mm, this will result in a model of 200 x 200 x 800 grid points (see Fig. 2). The concrete model is surrounded on each side with a layer of vacuum that is two grid points thick. In this layer, the velocities are set to zero while the density is set to a small but non-zero value to consider that the concrete specimen is surrounded by air.

For the simulations, a single source and a single receiver are used. Source and receiver are located at the center of the x-y-axis and separated in z-direction by 300 mm. The source is implemented as a six-component moment tensor source with only the xx- and zz-components being non-zero. This resembles the radiation characteristic of the used ultrasonic transducers [23]. Furthermore, the source signal itself is calibrated using measurements of transducer signals used in the laboratory experiment. The central frequency of the source signal is $f = 60\,\text{kHz}$; waveform and spectrum are displayed in Fig. 5 in Finger et al. [10]. The receiver records the average of the xx- and zz-components of the stress tensor. We use finite-difference operators with a length of two in time and in space and 80000, 160000, or 320000 time steps with a time increment of 5×10^{-8} s. This will result in a total physical time length of 4 ms, 8 ms, and 18 ms, respectively.

We have three different materials in our concrete models: the quartzitic aggregates (grains), mortar, and air inclusions. In our elastic model (no attenuation), we use the parameters of Vu et al. [32], summarized in Table 1.

In Appendix C, we explain how to derive the optimal parameters $y_1, y_2, \omega_1, \omega_2$ and τ for a viscoelastic constant Q approximation using Eq. 1. The following rules have to be applied using $c_{11} = v_p^2\rho$ and $c_{44} = v_s^2\rho$:

$$c_{xx} = \tau^2 c_{xx}, \tag{2}$$

$$\tilde{Y}_1^{xx} = y_1\,\tau^2\,c_{xx} \tag{3}$$

and

Table 1 Young's modulus E, Poisson's ratio ν, density ρ and p- and s-wave velocity v_p and v_s of the three different phases of our concrete model displayed in Fig. 2

Material	E	ν	ρ	v_p	v_s
Quartzitic aggregates	84.6 GPa	0.12	2670 kgm^{-3}	5723 ms^{-1}	3761 ms^{-1}
Mortar	21.45 GPa	0.19	2105 kgm^{-3}	3759 ms^{-1}	2325 ms^{-1}
Air inclusions (vacuum)	0.0 GPa	-	0.0001 kgm^{-3}	0 ms^{-1}	0 ms^{-1}

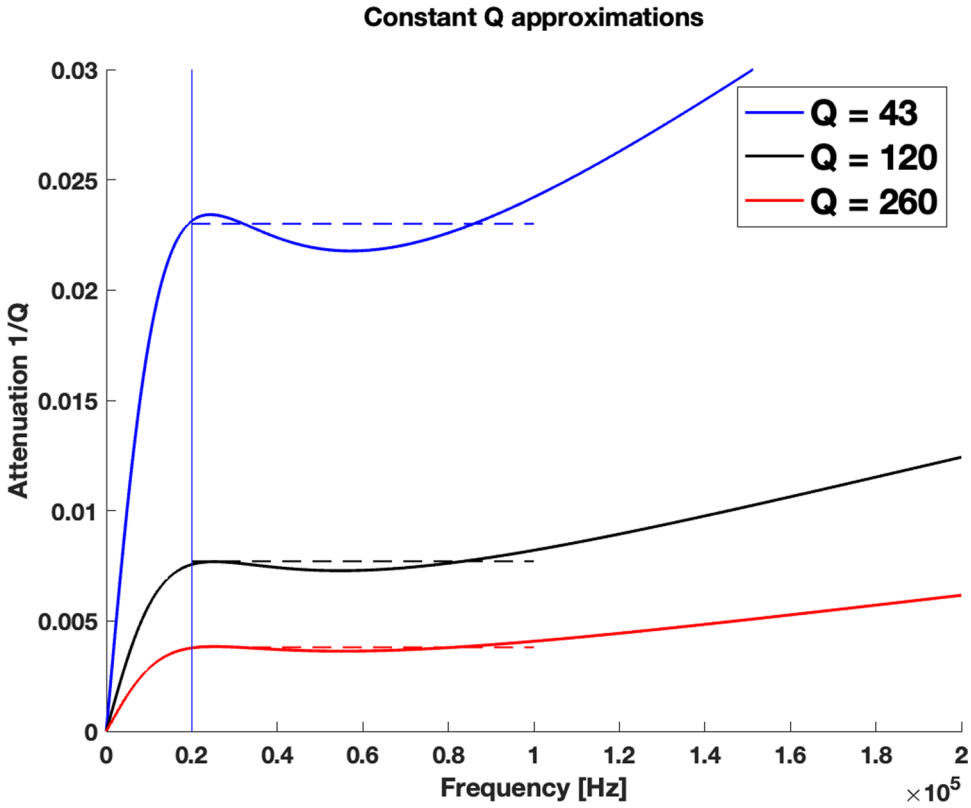

Fig. 4 Q approximations of the used finite-difference scheme. The corresponding parameters are given in Table 2. The dashed lines illustrate the range where Q should be constant

Table 2 The parameters y_1, y_2, and τ are used in Eqs. 2, 3, and 4 to calculate the elastic tensor and the tensors of anelastic coefficients of Eq. 1

Q approximation	y_1	y_2	τ
43	0.033	0.145	1.0868
130	0.012	0.055	1.0309
260	0.0062	0.028	1.0151
Infinity (no attenuation)	0	0	1

Equation 1 defines the anelastic behavior employed in the numerical scheme

$$\tilde{Y}_2^{xx} = y_2 \, \tau^2 \, c_{xx}. \tag{4}$$

To approximate a constant Q in the frequency band from 20 kHz to 100 kHz for all single material phases of the simulation, we consistently employ two Maxwell bodies with $\omega_1 = 2\pi \times 20\,\text{kHz}$ and $\omega_2 = 2\pi \times 1000\,\text{kHz}$. Utilizing a single Maxwell body proves inadequate for achieving a sufficient constant Q approximation. Conversely, incorporating more than two Maxwell bodies introduces high computational costs, making such an approach impractical. This balanced selection of two bodies effectively addresses both accuracy and efficiency within our simulations.

In this study, we performed four simulations: A fully elastic simulation without any intrinsic attenuation and three simulations with a constant Q approximation of 43, 130, and 260 (illustrated in Fig. 4). The values of y_1, y_2 and τ for the different Q values are given in Table 2. A snapshot of the wavefield (z-displacement) is shown in Fig. 5.

 https://doi.org/10.1007/s43452-025-01412-2

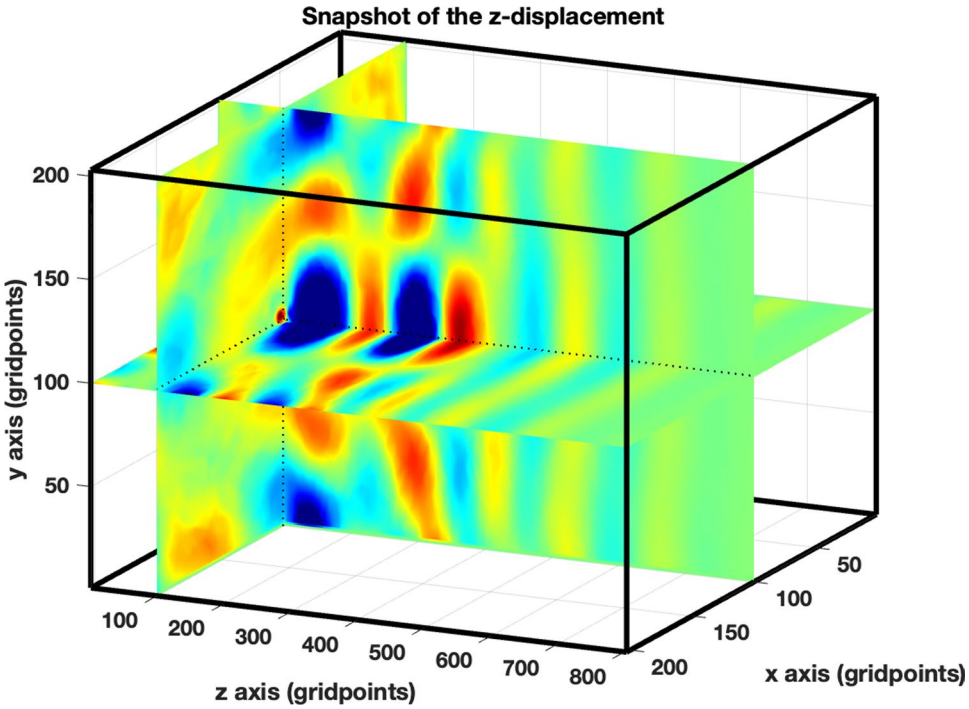

Fig. 5 Snapshot of the z-component of the displacement field simulated using the digital model

4 The determination of Q for concrete step by step

4.1 Experimental results

The ultrasonic recordings of the three saturation stages described in Sect. 2 are shown in Fig. 6. Two features can be observed qualitatively immediately: (1) The decay of the amplitudes seems faster for the saturated concrete (left hand side) compared to the dryer one (right hand side). (2) The absolute amplitudes are lower the more saturated the samples are. Please note that for the displayed time of $t = 0.0075\,\mathrm{s}$ a P-wave will propagate a theoretical distance of 38 m while the length of the concrete specimen is 0.4 m.

4.2 Numerical results

No attenuation

The simulated receiver data for the elastic simulation using the realistic digital twin including the scatterers but without intrinsic attenuation is shown in Fig. 7. Even after 16 ms the amplitudes will not significantly decline because the waves are trapped within the elastic model. In contrast to that, we observe in the laboratory experiments (see Fig. 6) that there is a significant amplitude decay. The wave field after 16 ms is a complex mixture of multiple reflected, scattered, and converted waves. Interestingly, in the beginning of the simulation (up to 2 ms), there is an observable decay of amplitudes. We interpret this behavior as a "wave saturation effect": After 2 ms, all waves are distributed statistically equal in the modeling domain, and the amplitudes will stay statistically constant. This is in contradiction to the experimental results. Therefore, one can conclude that the experimental observation can only be matched with the implementation of an intrinsic attenuation mechanism.

Q = 43

The simulated receiver data for the viscoelastic simulation with a Q-approximation of Q=43 is shown in Fig. 8. The signals of the recorded waves will decay relatively fast to zero. Here, the waves are attenuated due to the implemented Maxwell bodies. However, even a qualitative visual comparison with the experimental data leads to the conclusion that the numerically implemented attenuation of Q=43 is too strong to match the experimental

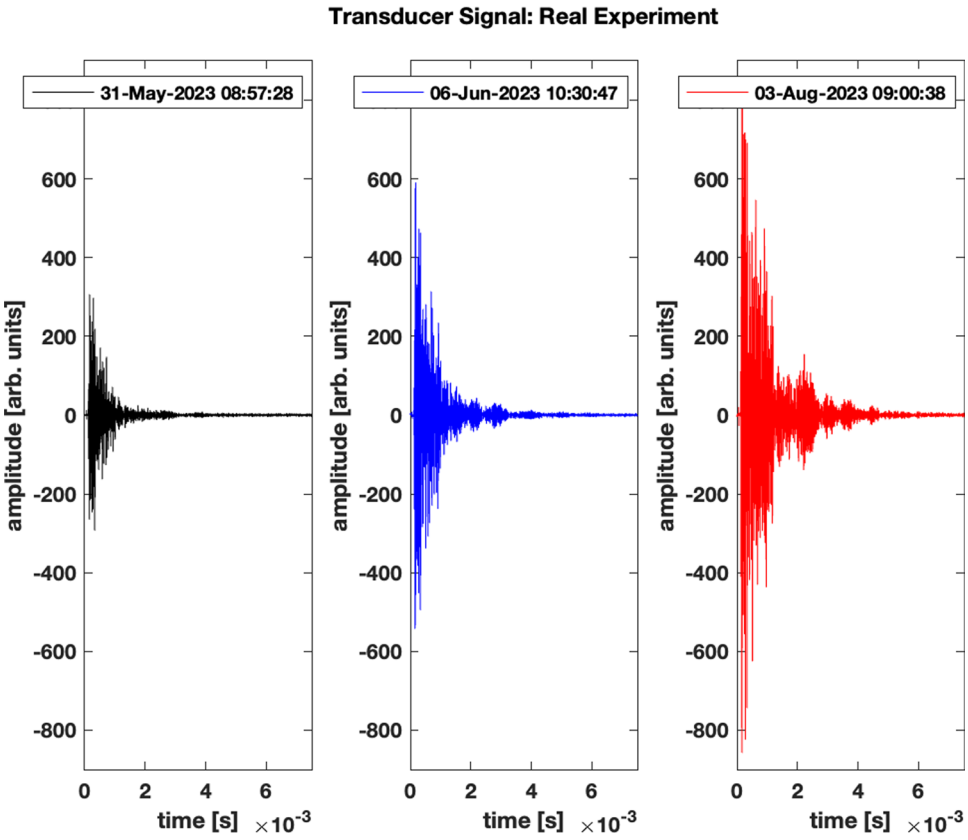

Fig. 6 Ultrasonic recordings of the laboratory specimen at the three saturating levels described in Sects. 2.4, 2.5 and 2.6. At the beginning of our experiment on 31 May 2023 we assume the specimen to be 100 % water-saturated

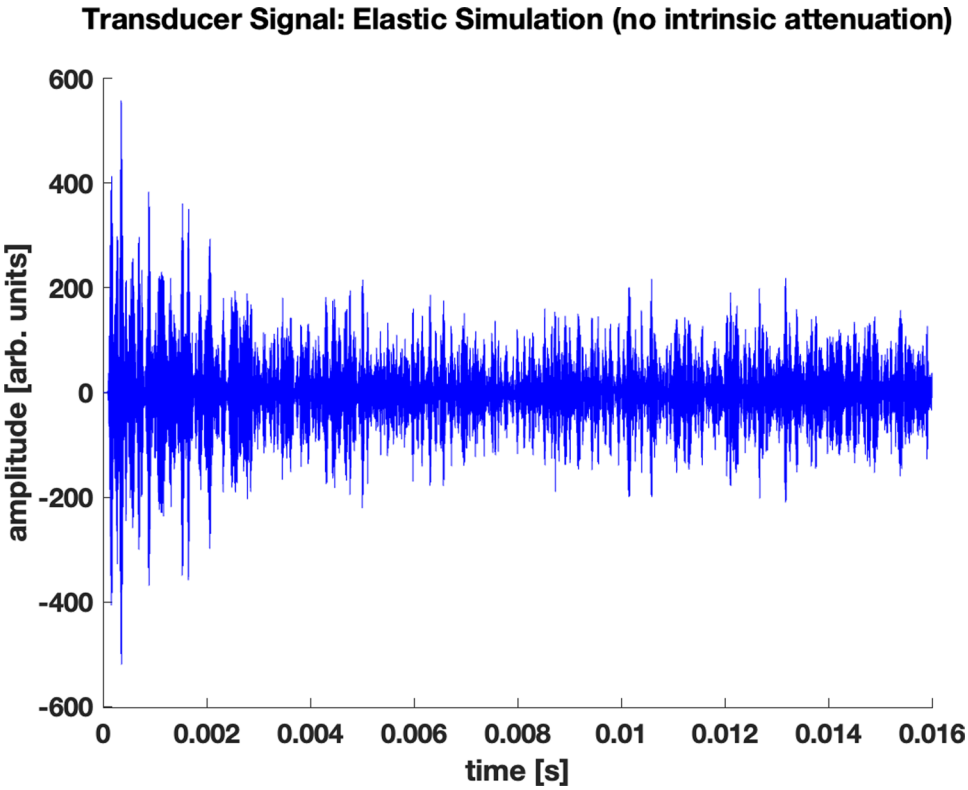

Fig. 7 Normalized receiver signal of the simulation with no intrinsic attenuation (details see text)

 https://doi.org/10.1007/s43452-025-01412-2

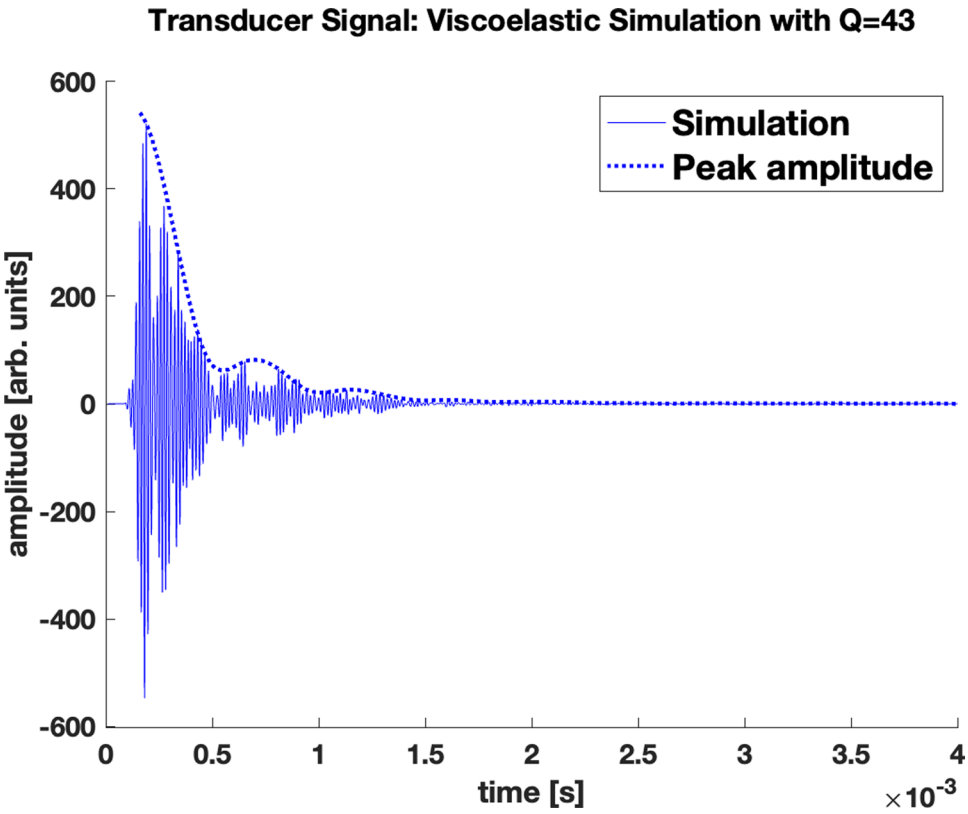

Fig. 8 Normalized receiver signal of the simulation with the described Q=43 approximation (details see text); the blue dotted line is the envelope of the peak amplitude

behavior for all cases displayed in Fig. 6. We can conclude that the value of the intrinsic attenuation Q of our concrete sample is higher than 43.

Q = 130

The simulated receiver data for the viscoelastic simulation with a Q-approximation of Q=130 is shown in Fig. 9. On a first look this simulated data looks similar to the experimental observation on 31.05.2023 (see Sects. 2.4 and 4.1). This seems to be the best fit to the initial condition with a high saturation level in the concrete specimen (To be confirmed in the next section).

Q = 260

The simulated receiver data for the viscoelastic simulation with a Q-approximation of Q=260 is shown in Fig. 10. At first look, this simulated data looks similar to the experimental observation on 31.05.2023 (see Sects. 2.6 and 4.1). This seems to be the best fit to the concrete specimen subjected to two months of drying (To be confirmed in the next section).

4.3 Determination of Q by comparison of simulations and experiment

We compare the peak amplitude envelopes of the simulations shown in Figs. 9 and 10 with the peak envelopes of the real experiments at different saturation levels (see Sect. 2.1). The key feature to observe is a similar decay of the amplitudes with respect to time. This decay is mainly due to intrinsic attenuation. The idea here is that the ultrasonic waves cannot escape from the acoustically isolated concrete sample. Scattering will only re-distribute the energy in the sample and will therefore not influence our observations significantly. For example, in 5 ms, which is typically the time we analyze, a P-wave can bounce back from one side to the opposite side of the sample more than 50 times. The observed good match for the Q=130-case with the recorded signal of the saturated concrete sample is displayed in Fig. 11. We, therefore, conclude that for our saturated concrete specimen, a Q factor of 130 is a good estimation of the intrinsic attenuation.

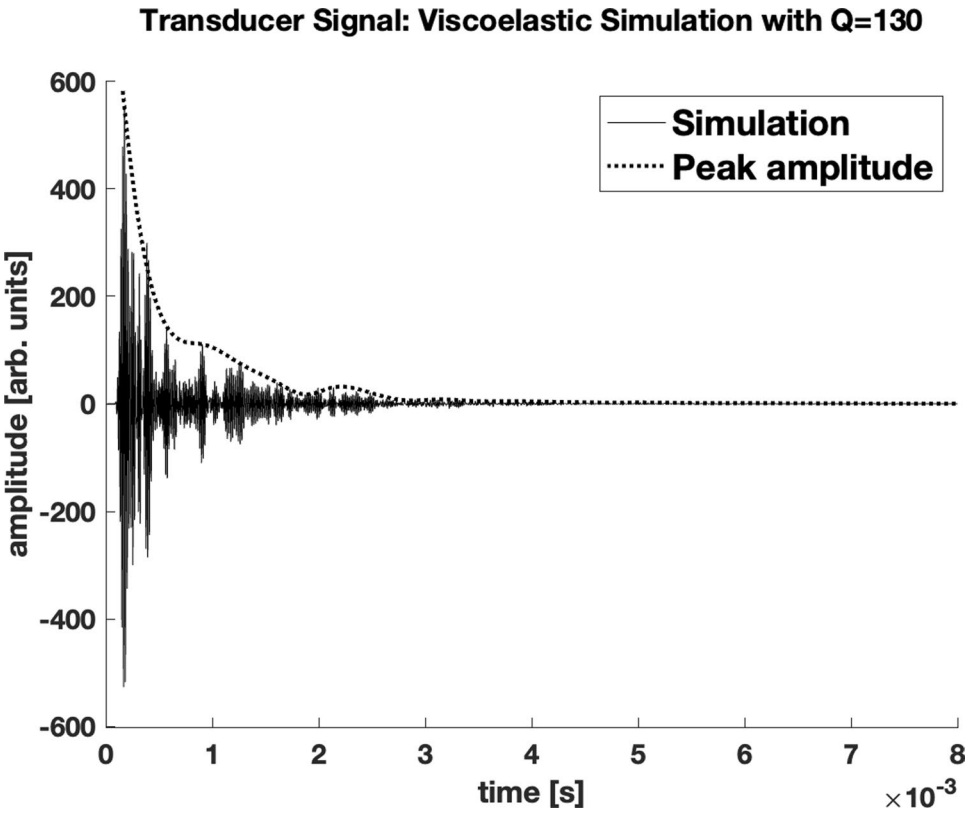

Fig. 9 Normalized receiver signal of the simulation with the described Q=130 approximation (details see text); the black dotted line is the envelope of the peak amplitude

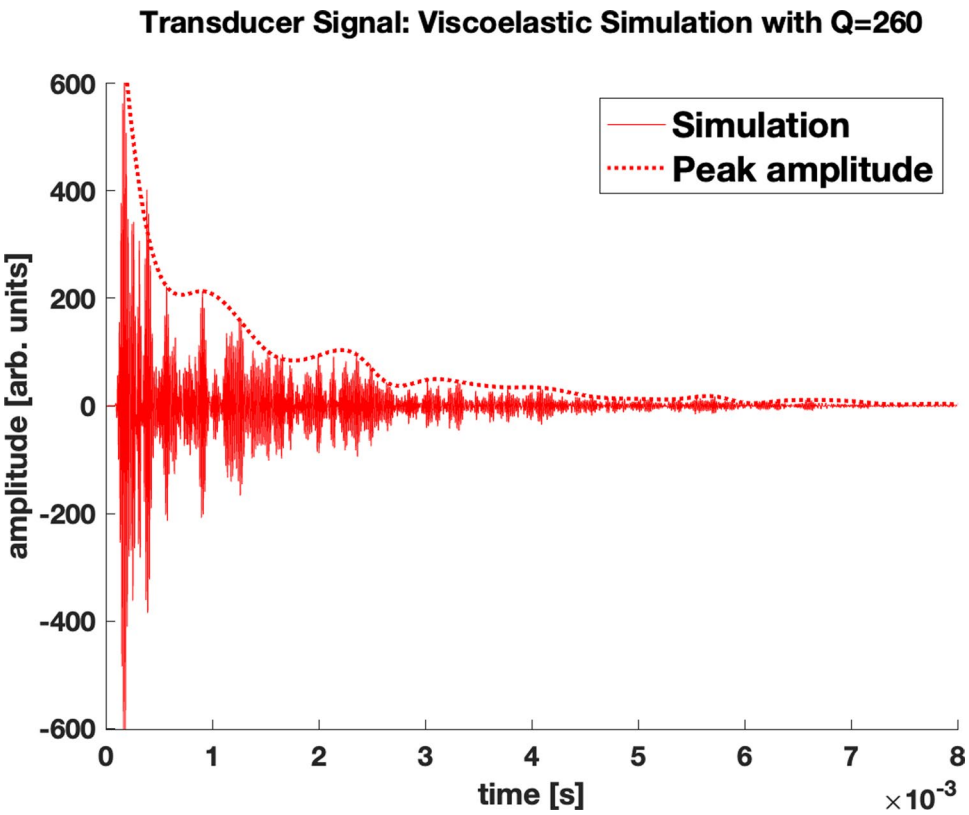

Fig. 10 Normalized receiver signal of the simulation with the described Q=260 approximation (details see text); the red dotted line is the envelope of the peak amplitude

 https://doi.org/10.1007/s43452-025-01412-2

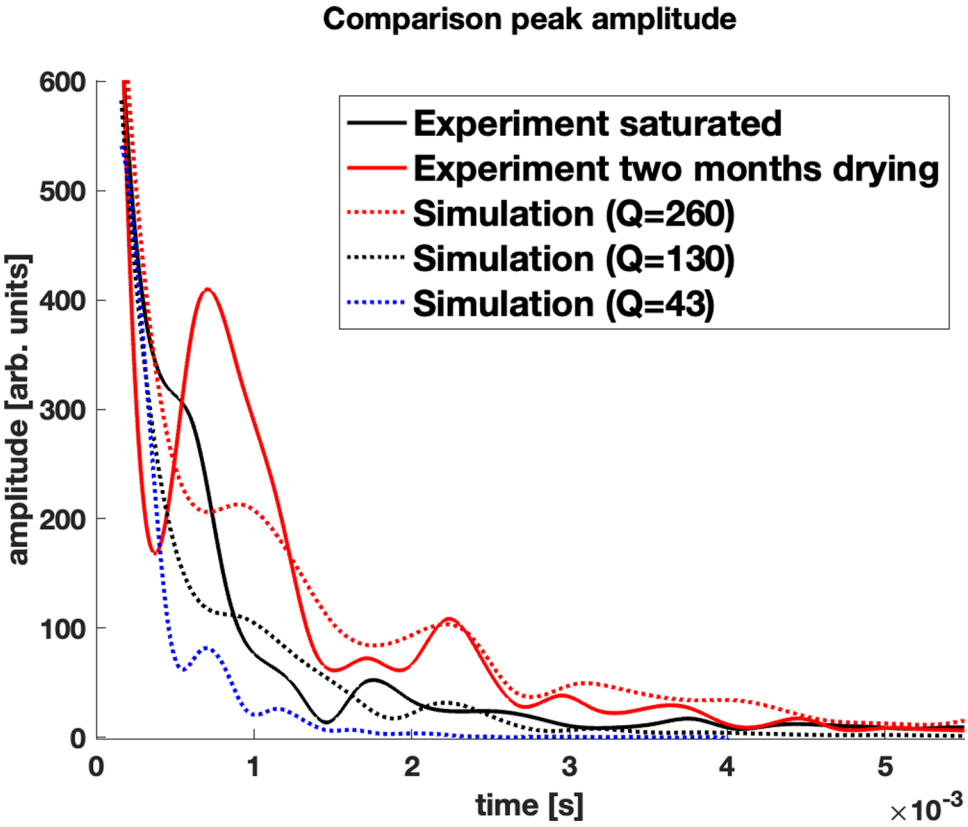

Fig. 11 Peak amplitude envelopes of the three simulations with Q=43, Q=130 and Q=260. The peak envelopes for the two experiments on 31.05.2023 ('saturated') and on 03.08.2023 ('2 months drying') are normalized to the same maximum amplitude to allow a comparison of the amplitude decay vs. time of all signals

The agreement of the envelopes of the numerical simulation using Q=260 with the experimental observation with the less saturated sample (see Sect. 2.6) is also relatively good. However, due to the relative complex drying process it remains unclear, what the internal humidity within the sample was at this point. However, our approach is able to determine the effective (i.e. average) Q-value for the total specimen. Therefore, we regard Q=260 more as a lower bound for a dry case.

5 Discussion

Achieving a perfectly identical digital reproduction of the initial experiment is exceptionally difficult. A key challenge lies in precisely matching the emitting sensor's radiation characteristics to the specific coupling with the sample, which itself represents a substantial research area. Therefore, a complete agreement between simulated and experimental signals is not anticipated. However, the approximations employed in our simulations provide a reasonable correspondence with the experimental results, enabling us to estimate the effective intrinsic attenuation of saturated and concrete samples with reduced internal humidity.

The following points would enhance the performed comparison further:

- The considered frequency band from 20 to 100 kHz is relatively broad. A more detailed study with individual relatively narrow frequency bands (e.g. narrow-band Gaussian-modulated pulses) should be considered to fully understand the intrinsic attenuation. However, in this study it is important that we have the best possible agreement between the source signal we have used in our laboratory experiment to the signal we used in our numerical simulations.
- The synthetic concrete structures could be replaced with segmented CT images (e.g. Landis et al. [18]) for more closely matching digital models.

- The exact shape and extent of the source and the receiver could be implemented in the digital model of the simulation.
- More Maxwell bodies should be implemented to have an even better match to the desired constant Q and a constant velocity. However, these would cause higher computational resources.
- In this study, we applied in the simulations the same intrinsic Q to the grains as well as to the mortar. Therefore, we estimate the effective Q of the concrete specimen. In the future, this can be assigned individually because it can be expected that the intrinsic attenuation in the mortar may be higher compared to the grains. However, this should be clarified in a separate study and is beyond the focus of this work. Also, a potential moisture gradient (e.g., see Sect. 2.6) could be implemented.
- Further, comparison of simulation results to experimental data collected from specimens with homogeneous internal moisture distribution should be carried out. Although these experiments take considerably longer than the one presented here, influences arising from moisture gradients could be excluded.

6 Conclusions

By comparison of viscoelastic simulations with experimental observations using a finite-size concrete specimen, we can estimate the intrinsic attenuation of concrete. We demonstrated that the performed experiment is a useful setup to determine this important quantity for the material characterization of concrete. For the saturated case, we determined a Q-factor of 130 in a frequency band around 60 kHz; for a sample that was dried for two months, we determined a Q-factor of 260.

Appendix A: Consecutive measurements of the used experimental dataset

The whole experimental dataset described in Sect. 2 can be found for all performed measurements in Jägle et al [13]. In Fig. 12 we demonstrate the high repeatability of the recordings for consecutive measurements. This is due to the fact that the embedded sensors will not be removed during the whole experiment. As explained above our method is based on the decay behavior at one single sensor (see e.g. Fig. 10). Therefore coupling effects of the sensors to the considered material can be neglected in our case.

Appendix B: Definitions of attenuation

Here, we briefly introduce different terms to characterize wave attenuation and their interaction. This will put the results of this paper into perspective to other published results. Following the description of Ono [24], the initial and attenuated wave amplitude in the displacement, A_0 and A, the propagation distance x and the attenuation coefficient α are related as follows:

$$A = A_0\, exp(-\alpha x). \tag{5}$$

The commonly used unit for α is dB m^{-1}. However, it is sometimes convenient to use Np m^{-1}, whereby 6.686 dB = 1 Np. Np stands for Neper, a non-dimensional unit. The attenuation coefficient α is related to the damping (or loss) factor η by $\eta = \alpha\lambda/\pi$, where λ is the wavelength and α is given in the unit of Np m^{-1} [24]. Here, $2\pi\eta$ is the ratio of energy dissipated per cycle to maximum energy stored per cycle; η is often denoted as Q^{-1} in seismology [19]. When η is independent of frequency, the attenuation coefficient α is given by Ono [24]:

 https://doi.org/10.1007/s43452-025-01412-2

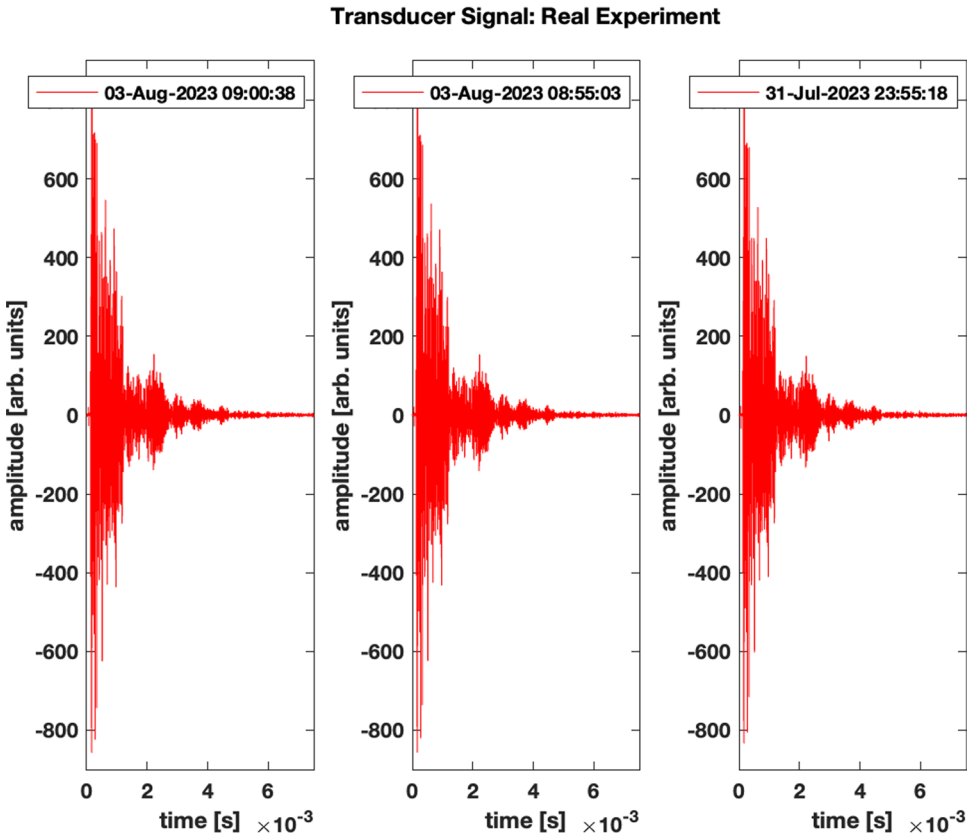

Fig. 12 Consecutive ultrasonic recordings of the real-life specimen at a similar saturating level. The recording on the left hand side is used in the analysis described above. The signal displayed in the middle is recorded five minutes before; the one on the right hand 3 days before

$$\alpha = \pi\eta/\lambda = \pi\eta f/v = \frac{\pi f}{Qv} \tag{6}$$

where f is the frequency and v is the wave velocity.

Appendix C: Approximation of a constant Q using two Maxwell bodies

The assumption of a constant Q is a widely used approach for describing seismic wave attenuation in rocks and concrete [24]. For linear viscoelastic systems, causality requires a fundamental relationship between velocity or modulus dispersion and Q; complete characterization of dispersion at all frequencies allows for determining Q and vice versa [21]. Therefore, we consistently plot wave dispersion and attenuation for each model. We begin with a single Maxwell body. Our objective is to match a constant P-wave velocity of $v_p = 5723\,\mathrm{m}s^{-1}$ (experimentally observed velocity in our concrete specimen) and a constant Q of 43 in the frequency band from 20 to 100 kHz. This initial attempt, displayed in Fig. 13, uses parameters $\omega_1 = 2\pi \times 60\,\mathrm{kHz}$, $c_{11} = (5800\,\mathrm{m}s)^2 \times 2670\,\mathrm{kg}m^{-3}$, and $\tilde{Y}_1^{11} = 0.05 \times c_{11}$ (Eq. 1). While this provides a starting point, the constant Q approximation proves inadequate, as evidenced by the deviation from the desired Q value. To achieve a more accurate match, we employ a two Maxwell body model. The workflow proceeds as follows:

1. **Frequency Range Definition:** Establish the desired frequency range (20 kHz to 100 kHz).
2. **Maxwell Body Frequencies:** Set the angular frequency of the first Maxwell body with the lower bound of the selected frequency range: $\omega_1 = 2\pi \times 20\,\mathrm{kHz}$; set the angular frequency of the second Maxwell body with a significantly higher upper bound of the selected frequency range: $\omega_2 = 2\pi \times 10 \times 100\,\mathrm{kHz}$.
3. **Initial Velocity and Density:** Initialize the effective velocity and density, $c_{11} = (5723\,\mathrm{m}s^{-1})^2 \times 2670\,\mathrm{kg}m^{-3}$.

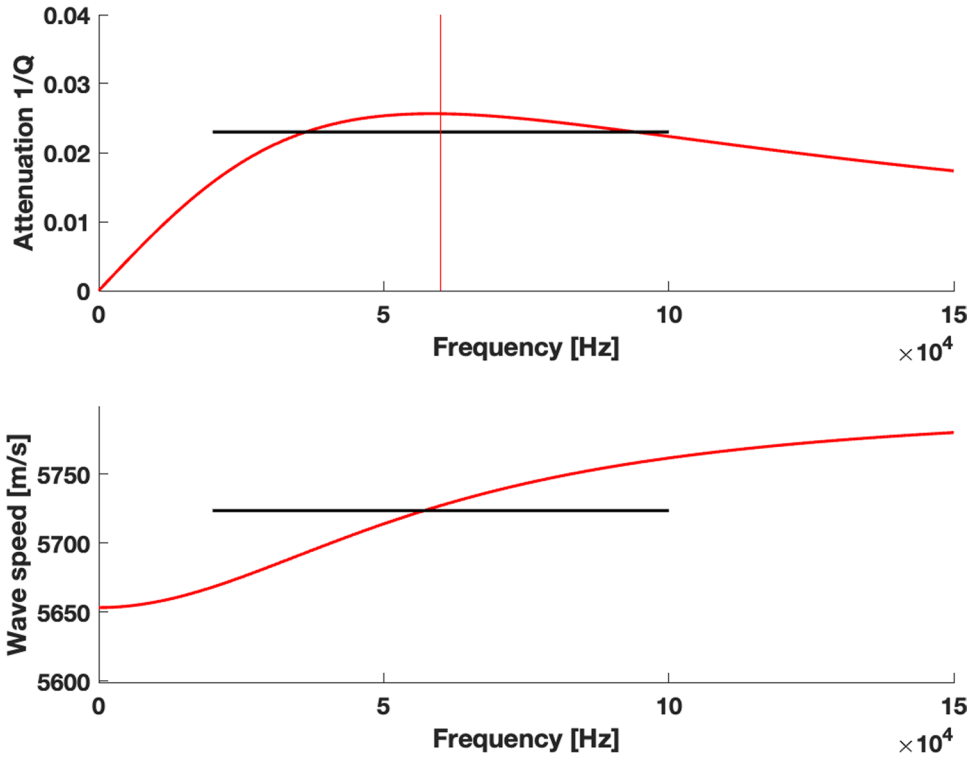

Fig. 13 One Maxwell Body: Attenuation and wave velocity versus frequency for a single Maxwell body model. The top panel displays attenuation, while the bottom panel shows the corresponding wave velocity. The red curve represents the modeled response, and the solid black horizontal line indicates the frequency range of interest, defining the frequencies where attenuation and velocity characteristics are optimized. This single-body model provides a baseline for understanding the impact of anelastic behavior on seismic wave propagation within the defined frequency band

4. **Attenuation Matching (First Body):** Adjust the first anelastic coefficient strength, $\tilde{Y}_1^{11} = y_1\, c_{11}$, to achieve the target Q value of 43 at the lower frequency bound (20 kHz). The second anelastic coefficient is initially set to zero: $\tilde{Y}_2^{11} = 0$.
5. **Iterative Optimization:** In step five, we adjust the second anelastic coefficient strength, $\tilde{Y}_2^{11} = y_2\, c_{11}$, to promote a more constant attenuation profile across the desired frequency band. This adjustment typically results in a slight increase in overall attenuation compared to step four. To mitigate this, we simultaneously fine-tune the first anelastic coefficient strength, y_1, decreasing it slightly. This simultaneous optimization of y_1 and y_2 promotes rapid convergence toward an optimal attenuation profile through iterative refinement; consecutive adjustments to y_1 and y_2 will quickly minimize deviations from the target attenuation behavior.
6. **Velocity Correction:** Finally, adjust the effective velocity to best match the experimentally observed P-wave velocity of $v_p = 5723\,\mathrm{m}s^{-1}$. This step maintains the optimized attenuation profile. The final result, shown in Fig. 14, yields $y_1 = 0.033$, $y_2 = 0.145$, and $c_{11} = (6220\,\mathrm{ms}^{-1})^2 \times 2670\,\mathrm{kg}m^{-3}$. We define τ as the factor by which the velocity is increased: $\tau = (6220\,\mathrm{ms}^{-1})/(5723\,\mathrm{ms}^{-1}) = 1.0868$.

   To calculate the frequency-dependent attenuation and wave velocity, we use the following equations:

$$1/Q_{xx}(\omega) = \Im\{C_{xx}(\omega)\}/\Re\{C_{xx}(\omega)\}, \tag{7}$$

and

$$v_{xx}(\omega) = \sqrt{\Re\{C_{xx}(\omega)\}/\rho}. \tag{8}$$

In this paper, a constant Q in the defined frequency band is the main priority; however, if a constant velocity is the main priority, the angular frequency of the first Maxwell body should be chosen lower than the lower bound of the chosen frequency band.

In our simulations in this paper, we also define an attenuation for the shear moduli. The anelastic coefficients $\tilde{Y}_1^{44}$ and $\tilde{Y}_2^{44}$ are derived with the same approach at the same angular frequencies.

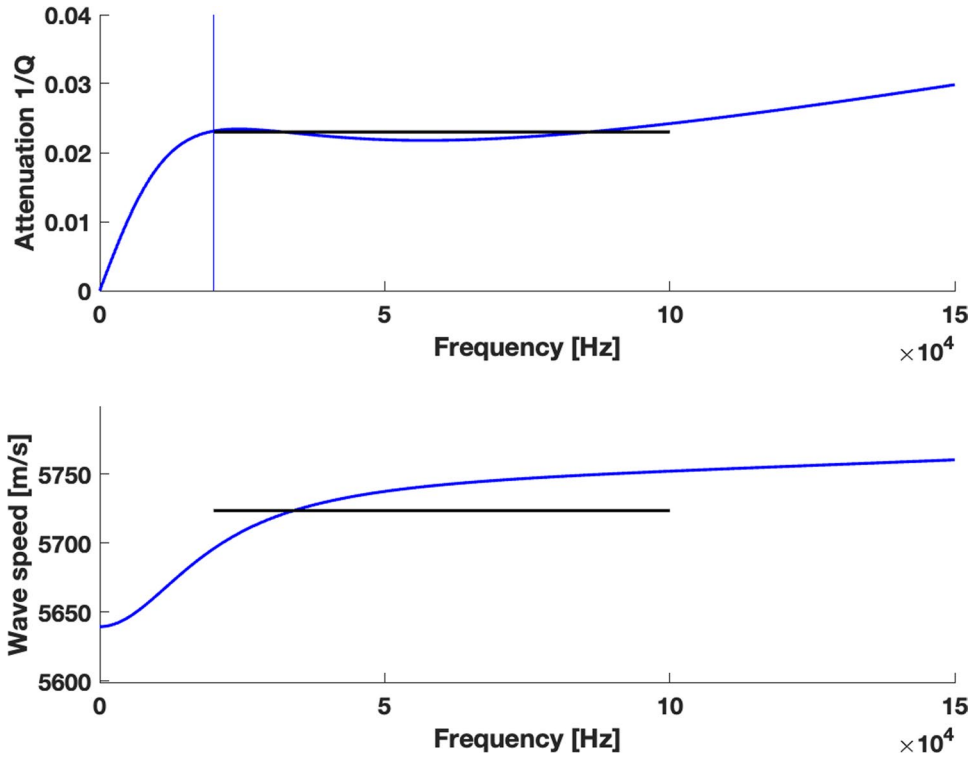

Fig. 14 Same as Fig. 13 but with two Maxwell Bodies: The blue curve represents the modeled response. The approximation for a constant Q and a constant velocity is improved in comparison to the case with one single Maxwell body

Acknowledgements The authors would like to thank the German Research Foundation (DFG) for their financial support in the framework of Subprojects BU, RUB1 and TUM1 of the Research Unit FOR 2825 (Project Number 398216472). EHS will thank the Deutsche Bahn for the additional time given to write this manuscript.

Funding Open Access funding enabled and organized by Projekt DEAL.

Data Availability Data sets of the current study are available from the corresponding author on reasonable request.

Declarations

Conflict of interest The authors have no conflict of interest to declare that are relevant to the content of this article.

Open Access This article is licensed under a Creative Commons Attribution 4.0 International License, which permits use, sharing, adaptation, distribution and reproduction in any medium or format, as long as you give appropriate credit to the original author(s) and the source, provide a link to the Creative Commons licence, and indicate if changes were made. The images or other third party material in this article are included in the article's Creative Commons licence, unless indicated otherwise in a credit line to the material. If material is not included in the article's Creative Commons licence and your intended use is not permitted by statutory regulation or exceeds the permitted use, you will need to obtain permission directly from the copyright holder. To view a copy of this licence, visit http://creativecommons.org/licenses/by/4.0/.

References

1. Abdullah A, Sichani EF. Experimental study of attenuation coefficient of ultrasonic waves in concrete and plaster. Int J Adv Manufact Technol. 2009;44(5):421–7. https://doi.org/10.1007/s00170-008-1840-7.
2. Ahn E, Song H, Shin M, et al. Influence of moisture on the diffusion of ultrasound in concrete. Ultrasonics. 2025;147:107529. https://doi.org/10.1016/j.ultras.2024.107529.
3. Barroso DF, Epple N, Niederleithinger E. A portable low-cost ultrasound measurement device for concrete monitoring. Inventions. 2021;6(2):36. https://doi.org/10.3390/inventions6020036.

4. Becker J, Jacobs LJ, Qu J. Characterization of cement-based materials using diffuse ultrasound. J Eng Mech. 2003;129(12):1478–84. https://doi.org/10.1061/(ASCE)0733-9399(2003)129:12(1478).
5. Chekroun M, Marrec LL, Lombard B, et al. Comparison between a multiple scattering method and direct numerical simulations for elastic wave propagation in concrete. In: Leger A, Deschamps M, Editors. Ultrasonic wave propagation in non homogeneous media. Springer Berlin Heidelberg, Berlin, Heidelberg; 2009, pp. 317–27. https://doi.org/10.1007/978-3-540-89105-5_28.
6. Cheyne AS, Thurman HO. Increasing the sound absorption coefficient in concrete. H-SC J Sci. 2022;11. https://blogs.hsc.edu/sciencejournal/wp-content/uploads/sites/6/2022/04/Cheyne-compressed.pdf
7. Diewald F, Denolle M, Timothy JJ, et al. Impact of temperature and relative humidity variations on coda waves in concrete. Sci Rep. 2024;14(1):18861. https://doi.org/10.1038/s41598-024-69564-4.
8. Diewald F, Denolle M, Timothy JJ, et al. EN 12390-2 Testing hardened concrete—Part 2: making and curing specimens for strength tests; German version EN 12390-2:2019;2019.https://doi.org/10.31030/3045734
9. Emmerich H, Korn M. Incorporation of attenuation into time-domain computations of seismic wave fields. Geophysics. 1987;52(9):1252–64. https://doi.org/10.1190/1.1442386.
10. Finger C, Saydak L, Vu G, et al. Sensitivity of ultrasonic coda wave interferometry to material damage–observations from a virtual concrete lab. Material. 2021. https://doi.org/10.3390/ma14144033.
11. Holla V, Vu G, Timothy JJ, et al. Computational generation of virtual concrete mesostructures. Material. 2021;14(14):3782. https://doi.org/10.3390/ma14143782.
12. Iliopoulos S, De Smet L, Aggelis D. Investigating ultrasonic wave dispersion and attenuation in fresh cementitious materials: a combined numerical, analytical, and experimental approach. NDT E Int. 2018;100:115–23. https://doi.org/10.1016/j.ndteint.2018.09.005.
13. Jägle E, Heimgreiter B, Timothy JJ, et al. Drying of saturated cement paste and concrete: ultrasonic, gravimetric and strain measurements (dataset). Zenodo. 2025. https://doi.org/10.5281/zenodo.14793770.
14. Kim JY. Velocity of ultrasound diffusion in heterogeneous media and its applications. Ultrasonics. 2025;145:107476. https://doi.org/10.1016/j.ultras.2024.107476.
15. Kocur GK, Saenger EH, Vogel T. Elastic wave propagation in a segmented x-ray computed tomography model of a concrete specimen. Constr Build Mater. 2010;24(12):2393–400. https://doi.org/10.1016/j.conbuildmat.2010.05.013.
16. Kocur GK, Saenger EH, Grosse CU, et al. Time reverse modeling of acoustic emissions in a reinforced concrete beam. Ultrasonics. 2016;65:96–104. https://doi.org/10.1016/j.ultras.2015.10.014.
17. Kristek J, Moczo P. Seismic-wave propagation in viscoelastic media with material discontinuities: a 3d fourth-order staggered-grid finite-difference modeling. Bull Seismol Soc Am. 2003;93(5):2273–80. https://doi.org/10.1785/0120030023.
18. Landis EN, Hassefras E, Oesch TS, et al. Relating ultrasonic signals to concrete microstructure using x-ray computed tomography. Constr Build Mater. 2021;268:121124. https://doi.org/10.1016/j.conbuildmat.2020.121124.
19. Li A, Roberts R, Margetan FJ, et al. Study of the effect of microstructure on ultrasonic signal attenuation. AIP Conf Proc. 2001;557(1):1322–9. https://doi.org/10.1063/1.1373907.
20. Livitsanos G, Shetty N, Verstrynge E, et al. Numerical simulation of elastic wave propagation in masonry compared with acoustic emission experimental results. Arch Civ Mech Eng. 2020;20(1):17. https://doi.org/10.1007/s43452-020-00019-z.
21. Mavko G, Mukerji T, Dvorkin J. The rock physics handbook: tools for seismic analysis of porous media. 2nd ed. Cambridge: Cambridge University Press; 2009. https://doi.org/10.1017/CBO9780511626753.
22. Nakahata K, Kawamura G, Yano T, et al. Three-dimensional numerical modeling of ultrasonic wave propagation in concrete and its experimental validation. Constr Build Mater. 2015;78:217–23. https://doi.org/10.1016/j.conbuildmat.2014.12.049.
23. Niederleithinger E, Wolf J, Mielentz F, et al. Embedded ultrasonic transducers for active and passive concrete monitoring. Sensors. 2015;15(5):9756–72. https://doi.org/10.3390/s150509756.
24. Ono K. A comprehensive report on ultrasonic attenuation of engineering materials, including metals, ceramics, polymers, fiber-reinforced composites, wood, and rocks. Appl Sci. 2020;10(7):2230. https://doi.org/10.3390/app10072230.
25. Philippidis T, Aggelis D. Experimental study of wave dispersion and attenuation in concrete. Ultrasonics. 2005;43(7):584–95. https://doi.org/10.1016/j.ultras.2004.12.001.
26. Punurai W, Jarzynski J, Qu J, et al. Characterization of dissipation losses in cement paste with diffuse ultrasound. Mech Res Commun. 2007;34(3):289–94. https://doi.org/10.1016/j.mechrescom.2006.10.003.
27. Saenger EH, Shapiro SA, Keehm Y. Seismic effects of viscous Biot-coupling: Finite difference simulations on micro-scale. Geophys Res Lett 2005;32(14). https://doi.org/10.1029/2005GL023222
28. Saenger EH. Time reverse characterization of sources in heterogeneous media. NDT E Int. 2011;44(8):751–9. https://doi.org/10.1016/j.ndteint.2011.07.011.
29. Saenger E, Bohlen T. Finite-difference modeling of viscoelastic and anisotropic wave propagation using the rotated staggered grid. Geophysics. 2004;69(2):583–91. https://doi.org/10.1190/1.1707078.

30. Saenger EH, Gold N, Shapiro SA. Modeling the propagation of elastic waves using a modified finite-difference grid. Wave Motion. 2000;31(1):77–92. https://doi.org/10.1016/S0165-2125(99)00023-2.
31. Ulm FJ, Constantinides G, Heukamp FH. Is concrete a poromechanics materials?—a multiscale investigation of poroelastic properties. Mater Struct. 2004;37:43–58. https://doi.org/10.1007/BF02481626.
32. Vu G, Meschke G, Timothy JJ, et al. A virtual lab for damage identification in concrete using coda waves. In: Life-Cycle of Structures and Infrastructure Systems; 2023. CRC Press, pp. 1834–41. https://doi.org/10.1201/9781003323020.
33. Yu T, Chaix JF, Audibert L, et al. Simulations of ultrasonic wave propagation in concrete based on a two-dimensional numerical model validated analytically and experimentally. Ultrasonics. 2019;92:21–34. https://doi.org/10.1016/j.ultras.2018.07.018.

Publisher's Note Springer Nature remains neutral with regard to jurisdictional claims in published maps and institutional affiliations.

Authors and Affiliations

Erik H. Saenger[1,2,3] · Martin Balcewicz[1] · Giao Vu[3] · Eva Jägle[4] · Jithender Timothy[4] · Claudia Finger[2]

✉ Erik H. Saenger
erik.saenger@hs-bochum.de

Martin Balcewicz
martin.balcewicz@hs-bochum.de

Giao Vu
giao.vu@ruhr-uni-bochum.de

Eva Jägle
e.jaegle@tum.de

Jithender Timothy
jithender.timothy@tum.de

Claudia Finger
claudia.finger@ieg.fraunhofer.de

[1] Hochschule Bochum, Am Hochschulcampus 1, Bochum 44801, Germany

[2] Fraunhofer IEG, Am Hochschulcampus 1, Bochum 44801, Germany

[3] Ruhr-Universität Bochum, Universitätsstraße 150, Bochum 44801, Germany

[4] Technische Universität München, Lichtenbergstraße 2, Garching b. München 85748, Germany